Understanding Crack Formation in IN738 Alloy Fabricated by Laser Powder Bed Fusion and Heat Treatment Process

Sara Safizadeh

A Thesis

in

The Department

of

Mechanical, Industrial

and

Aerospace Engineering

Presented in Partial Fulfillment of the Requirements
for the Degree of Master of Applied Science (Mechanical Engineering) at
Concordia University
Montreal, Quebec, Canada

August 2024

CONCORDIA UNIVERSITY

School of Graduate Studies

This is to certify that the thesis is prepared

By: Sara Safizadeh

Entitled: Understanding Crack Formation in IN738 Alloy Fabricated by Laser Powder Bed Fusion and Heat Treatment Process

and submitted in partial fulfillment of the requirements for the degree of

Master of Applied Science (Mechanical Engineering)

complies with the regulations of the University and meets the accepted standards with respect to originality and quality.

Signed by the Final Examining Committee:

_____ Chair

Dr. Martin D. Pugh

_____ Examiner

Hang Xu

_____ Examiner

Mamoun Medraj

_____ Supervisor

Dr. Tsz-Ho Kwok and Dr. Rolf Wuthrich

Approved by _____

Dr. Martin D. Pugh, Chair of Department or Graduate Program Director

_____ _____

2024 *Dr. Mourad Debbabi, Dean of Faculty*

Abstract

Understanding Crack Formation in IN738 Alloy Fabricated by Laser Powder Bed Fusion and Heat Treatment Process

by Sara Safizadeh

Cracking often occurs after Laser Powder Bed Fusion (LPBF) due to residual stresses from the manufacturing process. To mitigate these stresses, post-processing methods like stress relief Heat Treatment (HT) are used. This study combines computational and experimental methods to analyze and predict macro crack behavior in two geometries—dog bone and cruciform—fabricated from LPBF IN738 alloy. The objective is to understand and predict macro crack formation following LPBF and HT to prevent cracking. A coupled thermomechanical analysis was conducted to identify locations and timing of stress concentrations in the geometries. A simulation workflow was developed quantifying residual stresses at various stages of LPBF and HT. Fracture analysis using the stress intensity factor, a parameter in fracture mechanics, was performed to predict crack formation. Both numerical simulations and experimental validations were employed to assess this approach's effectiveness. Results showed that the stress intensity factor at stress concentration sites exceeded IN738's fracture toughness, indicating potential cracks. Despite geometric differences, both geometries showed similar stress peak patterns and crack behavior. High stress concentrations were observed early in the build process, during HT, and after cooling. The study also examined the impact of post-process sequences, such as HT and base plate removal, on geometric accuracy. These findings provide insights for designing geometries to prevent cracking and emphasize the role of geometric features and process sequencing in optimizing additive manufacturing. Understanding the relationship between design, residual stresses, and process sequences aids in developing robust design strategies and post-processing techniques to enhance LPBF component designs.

Acknowledgements

I would like to thank everyone who supported me during my degree. Special thanks to my thesis advisors, Dr. Kwok and Dr. Wuthrich, for their invaluable guidance and encouragement throughout this research. Their expertise has shaped this thesis significantly.

I am also thankful to Mitch Kibsey, Fabian Sanchez, and Mehdi Saboori for their assistance in various stages of this research project. Their contributions have greatly enriched the quality of this work.

Furthermore, I am grateful to my husband and family for their unwavering belief in me and constant encouragement. Their love and support have been my source of strength.

Lastly, I would like to acknowledge Siemens Energy for their generous financial support, which made this research possible.

Table of Contents

List of Figures

List of Tables

Chapter 1

Introduction

Additive Manufacturing (AM) processes is used in various industries such as aerospace, automotive, and turbomachinery due to their ability to enhance strength-to-weight ratio, reduced manufacturing leading time, and its capability to customized based on customer's demands [1], [2]. Additive manufacturing offers substantial advantages including overall reduction of cost and weight through shape optimization and the ability to fabricate complex geometries. One prevalent metal AM technique is Laser Powder Bed Fusion (LPBF), which utilizes a laser to systematically scan layers of spread powder based on the digital model's cross-section until the part is fully fabricated. LPBF involves rapid melting and solidification of metal powder, resulting in shrinkage and residual stresses, particularly problematic in materials with high carbon content. The residual stresses remaining in the fabricated component can possibly lead to deformation or crack, with cracks ranging from micro to scale. Macro cracks are more critical, as their larger size poses a greater risk compared to micro cracks. To mitigate these issues, many employ post-LPBF stress relief heat treatment (HT) to homogenize the microstructure and alleviate stresses [3]. However, HT presents its own challenges; the heating and cooling phases can propagate existing cracks or even initiate new ones. Consequently, it is crucial to develop a thorough understanding of the timing and mechanisms underlying macro crack formation to prevent design flaws. One approach to gain insight is through physical experimentation. However, directly observing these processes within the material during manufacturing poses challenges. While microscopy allows for post-formation crack analysis, it only provides insight into crack locations, not their timing or causation. The intricate relationship between heating and residual stress during processes like LPBF and stress relief HT cannot be fully understood through experimentation alone. To overcome this limitation, researchers often complement physical experiments with computational modeling and numerical simulation[4]. By simulating stress distribution throughout the heating and cooling cycle, the macro crack formation can be predicted and studied at any point in time. However, existing literature primarily focuses on fracture simulation either on as-built samples or under applied external loads that induce cracking [5]. To the best of our knowledge, there is a gap in the

literature regarding numerical fracture analysis of IN738 fabricated by LPBF and HT. IN738, a nickel-based superalloy known for its exceptional properties, is commonly used in demanding aerospace and energy applications, making it the primary material of interest in this thesis.

Our study shows the frequent occurrence of noticeable macro cracks in IN738 samples after LPBF and stress relief HT. Due to the challenges mentioned earlier, it remains unclear when the cracks initiate and how they correlate with the processes. Answering these questions are the primary objective of this thesis, aiming to provide crucial insights for future enhancements. Despite both LPBF and stress relief HT involve heating and cooling phases, we observed notable differences in their heat transfer mechanisms. In LPBF, each layer's melting and solidification introduce residual stresses across the layers, whereas stress relief HT subjects the entire component to heating and cooling, resulting in thermal gradients and localized stresses attributable to varying thicknesses. Furthermore, while stress relief HT helps reduce LPBF-induced stresses during high-temperature soaking, the subsequent cooling phase reintroduces new residual stresses. Building upon this observation, we hypothesize that the residual stresses after LPBF and stress relief HT differ, potentially resulting in varied crack formations. To test this hypothesis, an integrated process for simulating both LPBF and HT processes are constructed in order to quantify residual stresses in the samples. The calculated magnitude and distribution of residual stresses serve as valuable indicators for assessing part fracture.

In particular, a comprehensive simulation model was conducted to accurately calculate residual stresses during the entire manufacturing process. This involved characterizing the material properties of the IN738 alloy and integrating them into the model. Manufacturing parameters and boundary conditions were carefully defined to reflect real-world conditions. The simulation covered both LPBF and stress relief HT process, with LPBF modeling each layer deposition, laser melting, and solidification, while stress relief HT simulated the heating and cooling cycles of the entire part. Quantitative analysis was conducted to assess both the magnitude and distribution of residual stresses, with stress maps generated to visualize their distribution across the samples. Crack initiation locations and timing were identified based on the quantified stress concentration areas. The stress intensity factors at these initiation points were then calculated and compared to the critical fracture toughness. Cracks were identified where the stress intensity factor exceeded

the fracture toughness. Furthermore, the simulation results were compared and validated with physical samples, ensuring their accuracy and reliability. The thesis's contributions can be summarized as:

1. Development of a simulation workflow integrating IN738 alloy material properties to accurately quantify residual stresses at various stages of the LPBF and stress relief HT process

2. Detailed analysis of thermal stresses, stress distribution and crack initiation mechanisms throughout LPBF and stress relief HT operation

3. Validation of simulation results against physical samples to enhance understanding of the design and additive manufacturing processes, particularly in aerospace and energy applications.

The rest of the thesis is organized as follows. In Section 2, related works will be presented. Section 3 will outline the experimental setting and simulation methods. The simulation results and the evaluation of samples will be presented in Section 4. Finally, Section 5 includes analysis and discussion of experimental results, followed by a conclusion in Section 6.

Chapter 2

Literature review

2.1. Laser Powder Bed Fusion and Heat Treatment Process

Undesirable distortions and residual stresses often occur due to the sharp thermal gradients involved in the LPBF process, potentially leading to crack formation in additive manufactured samples. Various process parameters such as scan speed, laser power, build height, build plane area, and base plate condition, influence the distribution of residual stress and distortion. Zhang et al. [6] have demonstrated the significant impact of process parameters on crack susceptibility and mechanical properties, with findings showing that laser power and scanning strategies notably alter grain boundary morphology. As process parameters have a significant influence on the microstructure and residual stress, it is important to optimize the parameters to enhance the mechanical properties and reduce defects in Selective Laser Melting (SLM) components. Perevoshchikova et al. optimized the process parameters of the SLM process for IN738 by using Doehlert Design [7]. While optimizing process parameters can decrease residual stresses, as-built components often lack the required microstructure and mechanical properties. Therefore, post-processing methods are necessary to reduce residual stresses and address any remaining defects in the components [8]. Different post-processing techniques include shot peening (SP), laser shock peening (LSP), hot isostatic pressing (HIP), friction stir processing (FSP), and heat treatments (HT).

A considerable amount of literature has been published on the topic of AM post-processing [9]. A large number of these studies conducted the post-processes experimentally. For example, Greitemeier et al. [10] investigated the effect of post-HT and HIP processes on the fatigue performance of an additive manufactured TiAl6V4 component. One of the most effective ways to reduce residual stresses is the heat treatment process. Heat treatment, in particular, has been identified as one of the most effective ways to reduce residual stresses, with Nagesha et al. [11] showing significant reductions in tensile stresses through surface uniformity. Additionally,

Vrancken et al. [12] has highlighted the influence of heat treatment parameters, such as temperature, time, and cooling rate, on the microstructure and mechanical properties of SLM-produced materials like Ti6Al4V, emphasizing the importance of optimizing heat treatment conditions for desired material properties.

2.2. Numerical Simulation

Experimentally conducting post-processing procedures can be time-consuming and costly, particularly when issues such as unwanted distortion or cracking arise. Utilizing numerical simulations can offer a reliable means of design validation before actual testing. Several Finite Element (FE) simulation methods are available to predict the residual stress and distortion in parts produced through LPBF. These methods include weakly coupled thermomechanical, strongly coupled thermomechanical [13] and inherent strain method [14]. Modeling stress and distortion in LPBF needs substantial computational resources, especially for complex geometries. Research and commercial software like ANSYS commonly employ weakly coupled thermomechanical and inherent strain methods due to their accuracy and reasonable computational costs [15], [16]. For instance, Shrivastava et al. [16] demonstrated that increased dwelling time led to decreased component deformation with their implementation of a weak thermomechanical method.

Simulating post-processes can provide insights into how these processes affect distortion and stress distribution. While significant literature exists on laser shock peening (LSP) [17] Hot Isostatic Process (HIP) [18], relatively limited research has been published on HT processes following AM. Afazov et al. [19] simulated process chains using the FE methods, including oil quenching, aging, macro-scale machining, and shot peening. Recently, some studies have incorporated LPBF as the manufacturing process, followed by post annealing or heat treatment. For instance, O'Brien et al. [20] focused on the modeling process chain including AM, HT, LSP, and shot peening process for an impeller part made of IN718, with each FE process validated using experimental data. Similarly, Jin et al. [21] simulated the deformation and residual stresses of ALSI316L part fabricated by LPBF before and after annealing process, considering creep properties in the simulation. Lu et al. [22] studied the thermomechanical simulation of post heat treatment process for Ni-based GH4099 superalloy components fabricated by LPBF, investigating the effects of different heat treatment

conditions on residual stress relaxation. However, none of these studies have focused on IN738 fabricated using both LPBF and HT processes.

2.3. Fracture analysis

While research on residual stress in AM parts has been ongoing within the research community there is limited investigation into the fracture characteristics of AM materials. Existing research primarily focuses on fracture toughness, particularly on critical mode I plain strain stress intensity factor [23]. A large number of these studies used stress intensity factor to access fatigue properties due to the presence of defects and residual stresses in LPBF parts arises a major concern for fatigue performance in additive manufactured parts [24], [25], [26]. For example, Gruber et al. [27] investigated the effect of heat treatment and two stress ratios on the fatigue crack growth in LPBF sample, noting a higher fatigue crack growth rate with increased stress ratio. Additionally, predicting fatigue properties helps in better understanding of the service life of components manufactured by LPBF. Tang et al. [28] reviewed different models for predicting fatigue properties in metal AM components. Furthermore, Other studies have used standard fracture tests such as compact tension specimens to evaluate the plane strain fracture toughness [29]. Research on the effect of process parameters on fracture toughness of the LPBF-fabricated samples have also been conducted. Fielden and Davies [30], for example, studied on the effect of crack introduction on residual stress distribution in stainless steel samples, revealing a significant increase in tensile stress at the crack tip after initiation. While experimental investigations remain a common approach to characterizing fracture in AM components, these methods are often time-consuming and costly. As a result, simulations serve as a practical alternative for investigating various parameter combinations. However, there is limited research on predicting cracking in-process of LPBF in AM samples. Tran et al. [31] proposed an effective method to determine the critical j-integral, a measure of the strain energy release rate used to predict crack growth in material, of as-built additive manufactured part, utilizing simulations to identify cracks in LPBF-printed samples. Validation was conducted after LPBF using Xray diffraction (XRD) measurement, demonstrating the effectiveness of the J-integral method for characterizing cracking in LPBF materials [32]. To the best of our knowledge, there is no study on fracture parameters of LPBF-processed Inconel 738.

Chapter 3

Methodology

3.1. Introduction

This section explains the experimental method to fabricate samples, heat treat process and materials setups. Additionally, the numerical method used to predict deformation and evolution of stresses after LPBF process and HT process is detailed. Then, the fracture analysis done to find the crack locations is explained.

3.2. Materials and Experiment Setup

All the samples were fabricated by a metal AM printer – EOS M 290 (Krailling, Munich). IN 738 alloy was printed using the machine's suggested settings. The chemical composition (wt.%) was measured as follow: Ni-61.39, Cr-16, Co-8.5, Al-3.45, Ti-3.4, W-2.6, Mo-1.75, Tq-1.75, Ta-1.4, Nb-0.85, C-0.11 [33]. The material properties of Inconel 738 used in this study are referenced from references [33] and [34]. A wrought Stainless-steel plate was used as the base plate.

In this study, two geometric shapes are fabricated. The first geometry is a modified dog bone shape sample, and the second geometry is a cruciform shape sample. These geometries serve as a validation benchmark and are presented in Fig. 3.1 and Fig. 3.2. After the samples were fabricated, the samples were placed in the furnace for heat treatment process. The base plated was attached to the part for both samples during the post HT process.

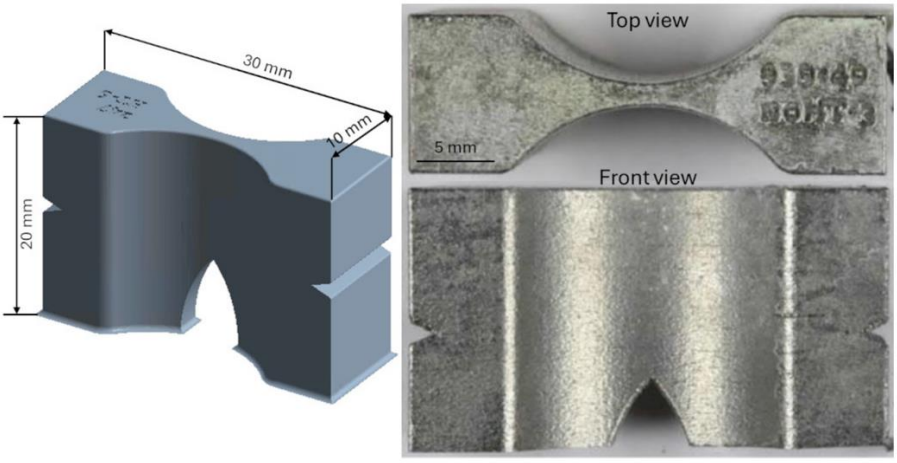

Figure 3-1. Modified dog bone shape geometry: digital model and physical sample

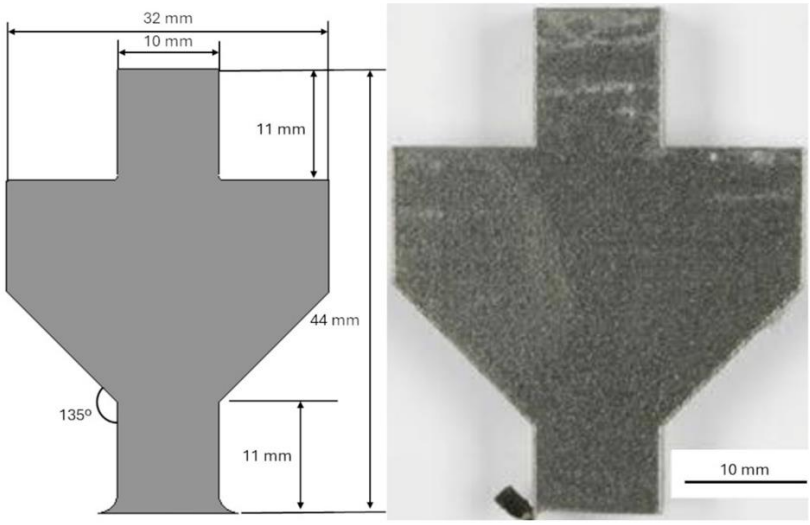

Figure 3-2. Cruciform shape geometry: digital model and physical sample

The heat cycle used for HT process begins with increasing the temperature to 1080 °C. The heating rate was considered 10 °C/min with the soaking time of 1 hour. After the HT process, the samples were removed from the base plate. The cracks were then observed and measured using Image J software, an open-source image processing software, from images taken from samples.

3.3. Simulation method

The simulation employs an integrated approach to predict deformation and stress evolution after the LPBF and HT process as shown in Fig. 3.3. It starts with the AM simulation, which involves coupled transient thermal and static structural analysis. The thermal analysis models the movement, power, and interaction of the heat source with the material, calculating the temperature profile as the material is melted, deposited, and solidified throughout the AM process. The structural analysis then uses these temperature distributions to determine the thermal stresses induced by temperature changes, such as expansion and contraction. It then assesses how these stresses cause deformation and evolve into residual stresses within the material. This process is coupled, meaning that the thermal results are continuously fed into the structural analysis to calculate stresses at each time step. Following the AM simulation, the HT simulation is performed.

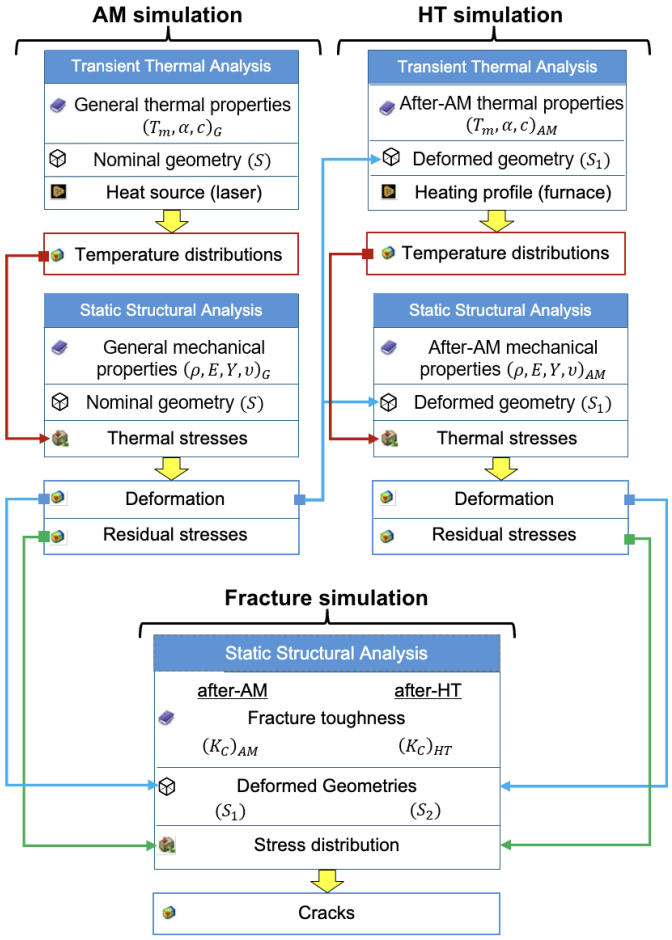

Figure 3-3. The simulation workflow, which includes an additive manufacturing (AM) simulation, a heat treatment (HT) simulation, and a fracture simulation

This simulation also includes thermal and structural analysis but uses the deformed geometry from the AM simulation and incorporates material properties relevant to the post-AM state. The thermal analysis in this stage models the furnace's heating profile, while the structural analysis calculates deformation based on the previously deformed geometry. Following each of these simulations, a fracture simulation can be conducted to assess potential crack formations for each step. Detailed descriptions of each simulation process are provided in the subsequent sections.

3.3.1. Laser Powder Bed Fusion (LPBF)

The LBPF process is simulated using Ansys Workbench 2022R1 [35] with the Additive Manufacturing module, which integrates laser heat source modeling and workflow automation tailored for simulating the layer-by-layer build process. Geometries are first converted into solid models in SCdoc format and then imported into Ansys for further processing. Meshing is crucial in additive manufacturing due to its layered nature and must ensure a consistent layer height. This process offers two main meshing options: Cartesian or layered tetrahedral methods, as the layer heights should remain consistent along the printing direction. For improved accuracy and due to the existence of sharp corners in both geometries, the dog bone and cruciform geometries use a layered tetrahedral mesh configuration [36]. Table 3.1 shows the mesh information used in this work. The mesh sizes are set to 0.8 mm for the part and 5 mm for the base plate. This distinction reflects their different roles, with the base plate mainly serving as a heat sink and fixed support.

Table 3-1. Mesh information

Samples	Mesh type	Element	Nodes	Mesh size build part(mm)	Mesh size base plate (mm)	Layer height (mm)
Dog bone	Layered Tetrahedrons	64852	104497	0.8	5	0.8
Cruciform	Layered Tetrahedrons	90712	136839	0.8	5	0.8

Within the simulation framework, the LPBF process is modeled using the element birth and death approach, a method commonly employed in such simulations. This method involves meshing the part and progressively adding layers to simulate the building process. To accurately capture the behavior of the material during manufacturing, various material properties are incorporated into the simulation. These properties, including density, coefficient of thermal expansion, melting temperature, modulus, Poisson's ratio, yield strength, thermal conductivity, and specific heat constant, are crucial for accurately representing the material behavior. It is worth noting that these material properties are temperature-dependent, meaning they change with temperature. Therefore, the temperature range of the imported material properties must extend from room temperature to the melting temperature to ensure successful simulation.

In addition to material properties, the simulation includes various process parameters such as laser power, scan speed, scan pattern, layer thickness, hatch spacing, and environmental conditions (e.g., build chamber temperature). These parameters are based on experimental settings and play a significant role in determining the outcome of the simulation. Thermal and structural boundary conditions are also carefully considered within the simulation. Thermal boundary conditions of AM process consider convection between the build plate and the gas chamber, as well as between the build plate and the surrounding un-melted powder during printing. The base plate temperature is considered 22°C. Structural boundary conditions dictate the part and base plate behave during cooling, with the bottom face of the base plate fixed throughout and the building part fixed to the base plate during the cool-down step

To optimize computational efficiency while maintaining accuracy, a weakly coupled thermomechanical analysis approach is utilized. This involves performing thermal analysis before structural analysis, assuming that each layer begins at its melting temperature without any initial strain. Subsequently, as the built layer undergoes cooling, thermal strains start to develop, and these temperature results are then used in static structural analysis to calculate displacement, stress, strain, and forces due to thermal strains. The general equation for this method is as follows:

$$\rho c_p \frac{\partial T}{\partial t} = \nabla(k.\nabla T) + Q \tag{3.1}$$

$$\varepsilon^{th} = \alpha(T - T_0) \tag{3.2}$$

$$\nabla\sigma = 0 \tag{3.3}$$

Where ρ is the density of material, c_p is the specific heat, T is the temperature at a point, k is the thermal conductivity, Q is the body heat balance that includes the heat delivered through the laser beam and thermal losses through radiation, convection or conduction. ε^{th} is the thermal strain, α is the thermal expansion coefficient and T_0 is the initial temperature at a point. The first equation calculates the temperature distribution in the material resulting from the heat source and thermal boundary conditions. The second describes the strain induced by temperature changes due to thermal expansion or contraction. The third equation represents the mechanical equilibrium condition. The mechanical model incorporates a constitutive model for elastic behavior using Hook's Law and plastic behavior through isotropic hardening rule. Finally, for the base plate removal process, three constrained points are selected to prevent any rigid body motion during removal. These points are chosen as close to the center as possible to ensure that, after removal, the part can deform as freely as possible. This careful consideration of technical details ensures the accuracy and reliability of the simulation results.

3.3.2 Heat treatment (HT)

The stress relief HT process is simulated within Ansys Workbench after the AM simulation. Practically, this can be streamlined by integrating a transient thermal analysis between the AM thermal analysis and the AM structural analysis as shown in Fig 3.4.

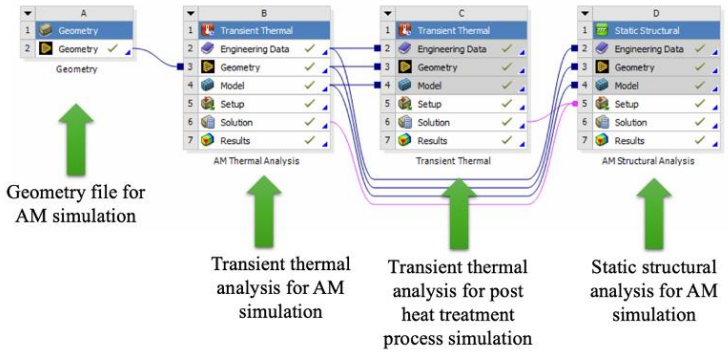

Figure 3-4. Schematic of the simulation workflow integrating geometry, AM transient thermal, HT transient thermal and AM static structural analysis

To simulate stress relief during HT, a relaxation temperature is considered. Typically, the relaxation temperature is set below the melting temperature. This allows strains to gradually

reduce, leading thermal strains to approach zero as the temperature nears the relaxation temperature. For IN738, the relaxation temperature is set to 850°C. The boundary condition for the HT process involves applying convection to both the base plate and the geometry itself.

3.3.3. Fracture

This study conducts a fracture analysis based on the residual stresses and deformation resulting from the AM and stress relief HT process. Residual stresses are crucial as they arise from the manufacturing and heat treatment processes and can significantly influence crack formation and propagation. Deformation is also considered to accurately represent the material's response and behavior. By using deformed geometry and residual stresses, the analysis mimics real experimental samples more closely. The methodology involves evaluating the maximum principal stress value obtained from the AM and stress relief HT analysis to identify the most probable instants of crack initiation. This process is necessary because crack initiation and propagation can occur at any point during both the AM and stress relief HT process. Therefore, evaluating stress at different stages of each process is crucial, rather than solely examining stress distribution at the final time step of each process. After identifying the crack initiation instances, the deformed geometry and residual stress data are exported for use in a fracture assessment analysis within ANSYS Workbench. To perform fracture analysis, it is essential to accurately transfer stress and deformation data into the fracture analysis because the fracture analysis results heavily depend on the accuracy of the residual stress data. Typically, this is achieved by linking the solution from the previous analysis to the setup of the subsequent analysis. However, with the additive manufacturing module in Ansys, direct linking is not feasible. To address this challenge, a three-step process is presented for transferring data from the additive manufacturing analysis to another analysis. Firstly, both the build part and base plate are exported to a CDB mesh file, ensuring precise mapping of node-based data to the same mesh and node ID. Subsequently, normal and shear stress values, along with deformation data based on node ID, are exported to separate Excel files. Finally, all exported files are imported as external models and data to establish a connection with a static structural analysis. For more detail on how to export CDB mesh file refer to appendix.

Ansys uses a critical maximum principal stress value as the criterion for fracture simulation [35]. In this context, cracks resulting from residual stresses are classified as static cracks. The simulations assume brittle fracture behavior with negligible plastic flow at the crack tip. Consequently, the stress intensity factor (K) method is applied to evaluate fracture parameters. The fracture properties for IN738 are calculated based on the mechanical properties of IN738. A crack is considered to occur when the stress intensity factor (K) exceeds the material's fracture toughness, the critical value of stress intensity factor.

Currently, there is no standard method for measuring fracture toughness in LPBF samples. In this study, fracture toughness is determined based on the prediction model of micro void coalescence fracture developed by Garrett and Knott [37]. Yu et al. [38] investigated the influence of HT on the fracture toughness of LPBF IN718 and validated the use of Garrett's prediction model for calculating fracture toughness in LPBF samples. Garrett's prediction model for fracture toughness ($K_{IC}{}^{*}$) is expressed by the following mathematical relationship:

$$K_{IC}{}^{*} = n\sqrt{\frac{2CE\varepsilon_f R_{p0.2}}{(1-\nu^2)}} \tag{3.4}$$

where C is a constant, E is the elastic modulus, $R_{p0.2}$is the 0.2% yield stress, ε_f is the fracture strain, n is the work hardening exponent, and ν is the Poisson's ratio. The values of these parameters are obtained from literature sources [33] and [40]. According to Zhou et al. [40], there exists a ratio (r_{exp}) between the calculated fracture toughness and the experimentally determined fracture toughness due to microstructural variations. Thus, the calculated value needs to be divided by this ratio to obtain the actual fracture toughness. All the variables and the final fracture toughness for LPBF and after HT process are summarized in Table 3.2.

Table 3-2. Material properties to calculate the fracture toughness $K_{IC}{}^{*}$

Parameter	**After LPBF**	**After HT**
n	0.073	0.13
C	0.025	0.25
E	205.07 GPa	205.07 GPa
$\mathbf{R_{p0.2}}$	822.15 MPa	700MPa

$\boldsymbol{\varepsilon_f}$	0.1135	0.06
$\boldsymbol{\nu}$	0.27	0.27
Cal. $\mathbf{K_{IC}}^*$	4176.1 MPa$\sqrt{\text{mm}}$	1508.4 MPa$\sqrt{\text{mm}}$
$\mathbf{r_{exp}}$	4.4	1.24
Exp. $\mathbf{K_{IC}}^*$	**949.11 MPa$\sqrt{\text{mm}}$**	**1216.21 MPa$\sqrt{\text{mm}}$**

Chapter 4

Results

This section presents the simulation results and compares them with the physical samples. All simulations were conducted using ANSYS Workbench 2022R1 on a PC running 64- bit Windows 10, equipped with an Intel Core i7-6700 CPU @ 3.40 GHz and 16 GB RAM.

4.1. Additive manufacturing simulation stress distribution

4.1.1. Dog bone sample

We will first examine the dog bone geometry illustrated in Fig 3.1. The temperature variations throughout the entire process are depicted in Fig. 4.1. During the AM build step, the temperature reaches peaks of 1260 ºC as new layers are sequentially melted and fused. Following this, an extended cooling period is allowed for the part to cool down completely. Finally, the HT step includes ramp-up, soaking, and cooling phases.

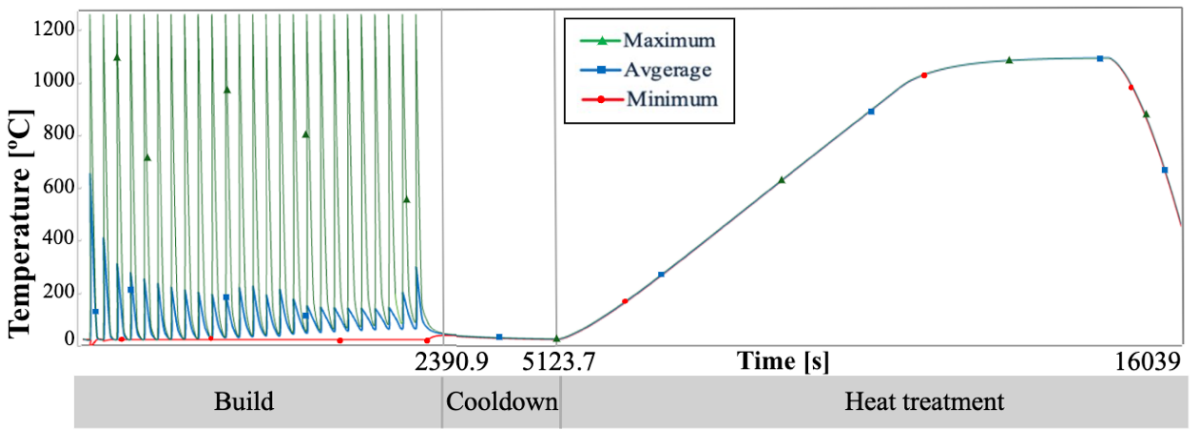

Figure 4-1. Temperature distribution graph for the dog bone geometry, showing maximum (△), average (■), and minimum (○) values across all mesh nodes

The variation of maximum principal stress throughout the entire process is illustrated in Fig 4.2. During the build step, stress fluctuates in response to temperature changes. Once the temperature stabilizes during the cooldown step, stress changes are minimal. In the HT step, the increase in temperature in the ramp-up phase leads to changes in stress. When the temperature reaches the relaxation temperature of 1080 ºC, the stresses fully relax. As the temperature decreases in the cooling phase, the maximum principal stress increases. These stress changes are attributed to the material's expansion and contraction under the given boundary conditions.

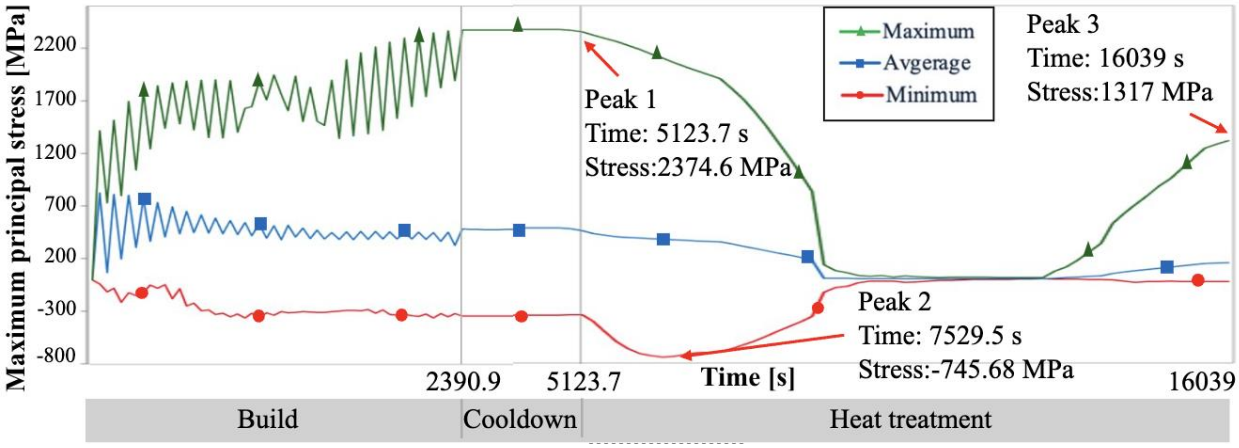

Figure 4-2. Maximum principal stress graph for the dog bone geometry, showing maximum (△), average (■), and minimum (○) values

The stress graph highlights several peak points:

- Peak 1 occurs at 5123.7 seconds, where the maximum principal stress reaches 2374.7 MPa at the side notch. This peak is due to changes in the cross-sectional area, which lead to stress concentrations.

- Peak 2 is observed at 7529.5 seconds during the ramp-up phase of the HT process, with a maximum principal stress of -745.68 MPa at the surface in contact with the base plate. The constraint from the base plate prevents thermal expansion, resulting in compressive stresses.

- Peak 3 is noted at 16039 seconds, at the end of the HT process, where the maximum principal stress is 1317 MPa at the bottom groove. As the part cools and shrinks, the base plate restricts the movement of the legs, inducing tensile stress at the bottom groove.

The peak points for the dog bone sample are shown in Fig 4.3.

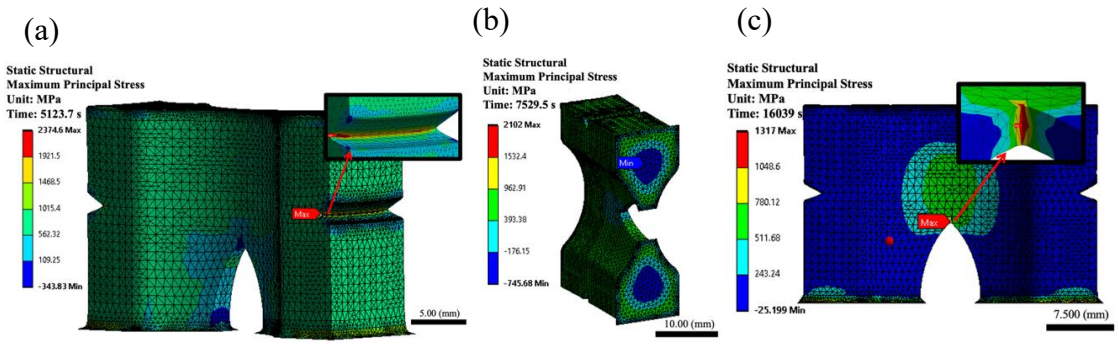

Figure 4-3. Maximum principal stress distribution of Dog bone sample (a) after LPBF of Dog bone sample (b) at the second peak of maximum principal stress (c) after HT

During the fracture simulation, the stress intensity factor (K) is calculated and compared to the fracture toughness (K_c), as detailed in Table 3.2. Peaks 1 and 3 were identified as locations for crack initiation. Specifically, at peak 1, the side notch exhibits a maximum K of 1361 MPa $\sqrt{mm}$, exceeding the KC after LPBF, which is 949.11 MPa $\sqrt{mm}$. At peak 3, the bottom groove indicates a maximum K of 1919.3 MPa $\sqrt{mm}$, surpassing the K_c after HT, which is 1216.21 MPa $\sqrt{mm}$. Fig 4.4 shows the actual cracks observed in the physical sample, and the simulated results align well with the physical observations in terms of crack locations.

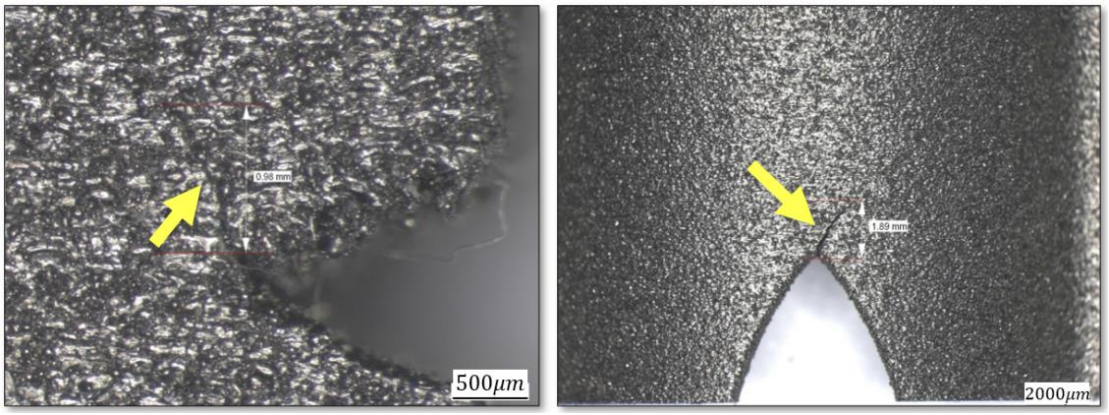

Figure 4-4. Actual cracks in the dog bone sample

It is important to recognize that the two cracks developed at different stages of the manufacturing process. The crack at the side notch formed after the LPBF phase, while the crack at the bottom groove emerged after the HT phase. Notably, the bottom groove experienced small compressive stress after LPBF, indicating that even similar features can exhibit distinct stress distributions based on their orientation. Therefore, addressing these cracks may require tailored approaches. For the side notch crack, strategies could involve optimizing build parameters or adjusting part orientation to reduce stress concentrations. In contrast, solutions for the bottom groove crack might focus on refining cooling protocols to alleviate residual stresses. Understanding the timing and origins of these cracks is crucial for developing effective mitigation strategies appropriate to each phase of the manufacturing process.

4.1.2. Cruciform sample

The thermal history of the cruciform geometry is similar to the dog bone geometry, as shown in Fig. 4.1. The important difference is that the cruciform geometry involves more layers, resulting in a longer build step, which concludes at 4664.4 seconds. The graph of maximum principal stress throughout the entire process is shown in Fig. 4.5.

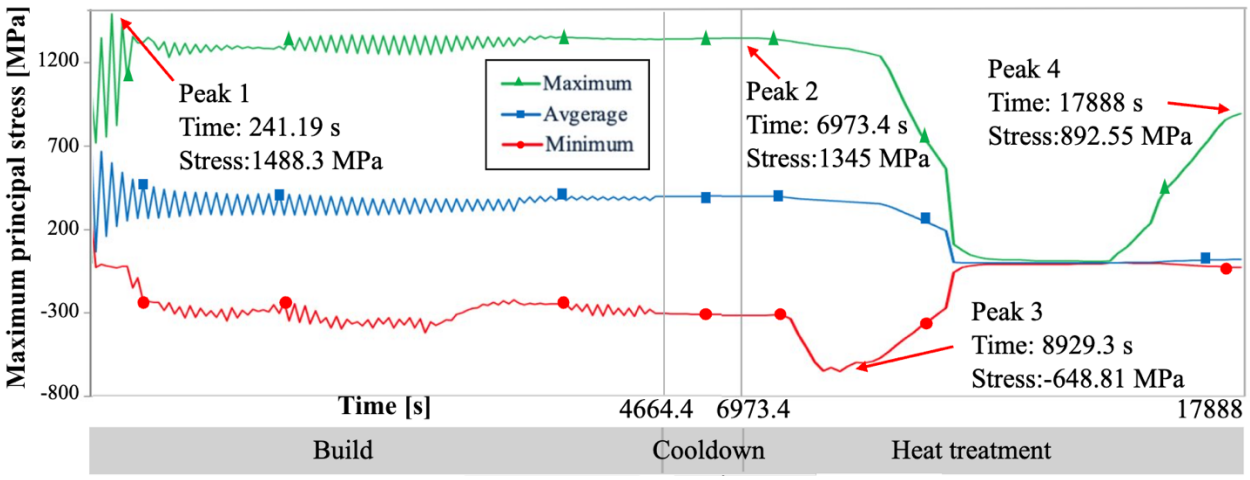

Figure 4-5. Maximum principal stress graph for the cruciform geometry, showing maximum (△), average (■), and minimum (○) values

The graph shows a trend similar to the dog bone geometry, with fluctuations during the build step, stabilization during the cooldown step, stress relaxation during the soaking phase, and an increase in stress during the cooling phase of the HT step. Peaks are observed at similar locations, with an additional peak appearing during the build step. To summarize:

- Peak 1 happens at 241.19 seconds, with the maximum stress recorded at 1488.3 MPa. At this stage, only a few layers have been printed, and the maximum stress is located at the interface between the part and the base plate.

- Peak 2 occurs at 6973.4 seconds after the LPBF process, with high stresses recorded at two locations: 1222 MPa at the top corner and 1300 MPa at the bottom corner.

- Peak 3 occurs at 8929.3 seconds during the ramp-up phase of the HT step, with the maximum principal stress of - 648.81 MPa located at the base.

- Peak 4 occurs at 17888 seconds after the HT process, with the maximum principal stress reaching 892.55 MPa, again at the base.

The peak points for the cruciform sample are presented in Fig 4.6.

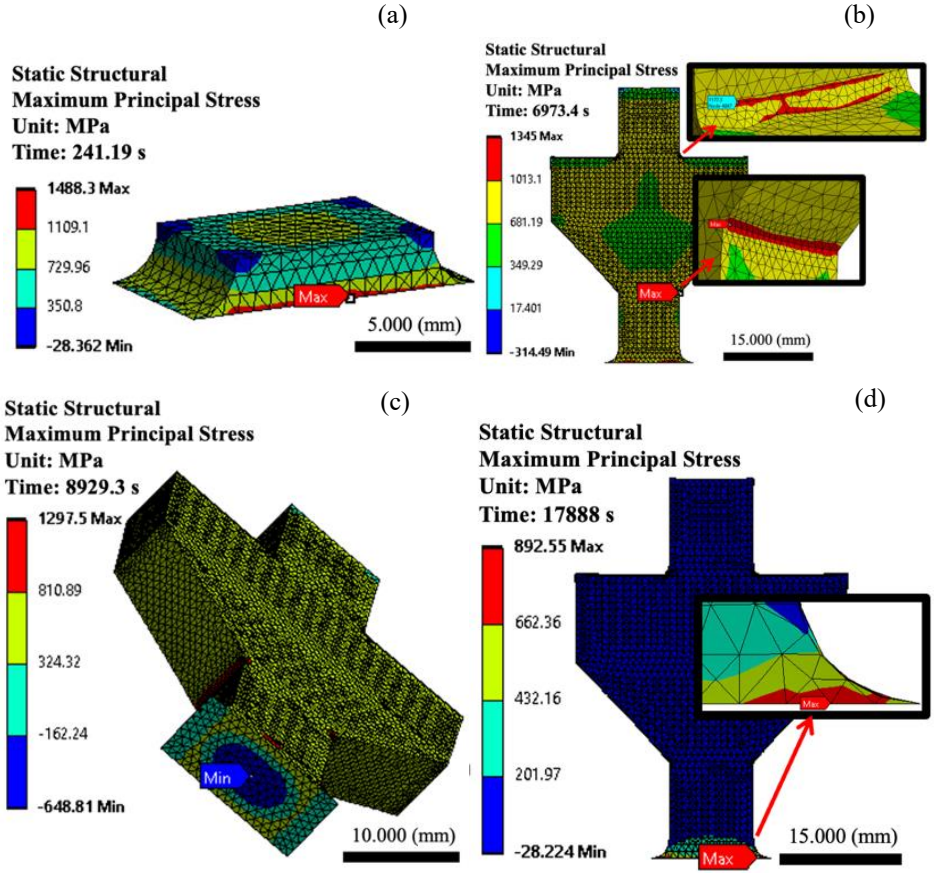

Figure 4-6. The maximum principal stress for the cruciform sample (a) at the first peak (b) after LPBF process (c) at the third peak (d) after HT process

The high stresses at the interface are less concerning because the part will eventually be detached from the base plate. Therefore, the primary focus is on peak 2, where the high-stress areas are located in the body of the part, which impacts its overall integrity. At this peak, the maximum stress intensity factors (K) are 1223.8 MPa $\sqrt{mm}$ at the top corner and 1294.5 MPa $\sqrt{mm}$ at the bottom corner. Both values exceed the fracture toughness (K_c) after LPBF, which is 949.11 MPa $\sqrt{mm}$. Because both cracks happen immediately after the LPBF phase, mitigation strategies for the cruciform geometry should primarily focus on the AM step, in addition to any modifications to the geometry itself.

Figure 4.7 illustrates the actual cracks observed in the physical sample. Unlike the simulation predictions, which indicated cracks at both the top and bottom corners, only a single crack is present at the top corner in the physical sample. We attribute this discrepancy to stress redistribution after the top corner crack initiates, which may have caused stresses initially predicted

for the bottom corner to contribute to the top crack instead. Additionally, it is crucial to consider that the quality of the physical samples significantly affects the observed crack patterns. Factors such as porosity and microcracks in the material can influence crack lengths and distribution. While simulations assume an ideal, defect-free scenario, the presence of such defects in the actual samples may lead to variations between observed and predicted crack lengths. These factors could also explain the absence of the predicted bottom crack in the physical sample.

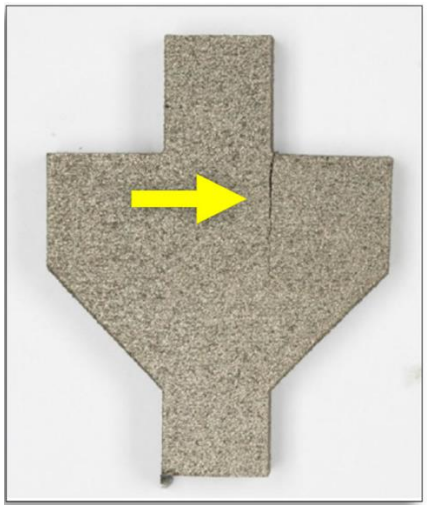

Figure 4-7. Actual cracks in the cruciform sample

Chapter 5

Discussion

This section presents a discussion of the results, aiming to provide a comprehensive understanding of simulating fracture analysis after LPBF and heat treatment. First, the geometry consideration will be discussed. Then, the timing of high stress peaks in both geometries are discussed. Lastly, we will present and discuss the effect of process sequence on the dimensional accuracy of samples.

5.1. Geometry Consideration

In evaluating the maximum principal stress results for the dog bone and cruciform geometries, it is clear that geometric design significantly affects the stress distribution and concentration. Both geometries show a unique characteristic that influences how stresses are distributed and where they peak, revealing important insights into their structural performance. The dog bone sample features a relatively uniform cross-section in each layer with notable V-grooves. The uniformity in cross-section generally contributes to a more predictable stress distribution across the part. However, the V-grooves introduce localized stress concentrations due to their sharp transitions, causing significant stress peaks at these regions. These localized features create points where stress intensity factors (SIF) exceed the material's fracture toughness, indicating potential sites for failure. The uniform cross-section helps reduce stress variations elsewhere, but the V-grooves remain critical areas for design focus to prevent high stress concentrations.

In contrast, the cruciform sample is characterized by its discrete cross-sections—small, large, and then small again—creating a step-like profile. This geometric variation results in stress concentrations, particularly at the transitions between different cross-sectional areas. While the cruciform design is less complex than more intricate geometries, the sudden changes in cross-sections introduce significant stress concentrations at these boundaries. These transitions act as

stress concentrators, similar to how V-grooves affect the dog bone geometry, but the nature of these concentrations is influenced by the step- like profile of the cruciform.

In summary, both geometries emphasise the importance of geometric design in influencing stress distribution and intensity. The dog bone's V-grooves and the cruciform's discrete cross-sections each create specific stress concentration points that must be carefully managed. Understanding and addressing these stress concentrations through thoughtful design and manufacturing adjustments are essential for improving the performance and reliability of both geometries.

5.2. Timing of High Stress Peaks

The timing of high stress peaks during the LBPF and HT process provides insight into how geometric features and thermal conditions influence stress distribution in both the dog bone and cruciform geometries. Interestingly, there are notable similarities in the timing and nature of their stress peaks. Both geometries show significant stress concentrations at critical points during the LBPF and HT process.

For the dog bone sample, a high stress peak occurs at 5123.7 seconds at the V-grooves, while the cruciform shows a significant peak at 6973.4 seconds at the top and bottom corners. These peaks highlight how specific geometric features—V-grooves in the dog bone and discrete cross-sections in the cruciform—introduce stress concentrations during the build process. As the process transitions into the HT phase, both samples show additional stress peaks that reflect the impact of thermal constraints. The dog bone reaches a peak at 7529.5 seconds due to compressive stresses from thermal expansion constraints imposed by the base plate. Similarly, the cruciform experiences a peak at 8929.3 seconds during HT ramp-up, showing compressive stresses at the base. These peaks, occurring in the same phase of the process for both geometries, emphasizing the role of thermal constraints in shaping stress distribution, regardless of geometric complexity.

In the end of cooling, both geometries indicate additional peaks. The dog bone shows a peak at 16039 seconds with tensile stress at the bottom groove, while the cruciform peaks at 17888 seconds with tensile stress at the base of the sample. These similar stress patterns during cooling step highlight how thermal contraction and geometric constraints affects stress distribution across different geometries.

In conclusion, despite the differences in geometric design, the similarities in stress peak timing and distribution across the dog bone and cruciform samples illustrate that the process sequences are also crucial in determining stress patterns. The interactions between geometric features and thermal processes play a significant role in shaping stress distribution, emphasizing the importance of considering both factors when optimizing design and manufacturing strategies.

5.3. Process Sequence

The decision of whether to remove parts from the base plate before or after HT is often a debatable topic in AM. The choice can have significant implications for deformation and part accuracy. On one hand, removing the part from the base plate before HT will cause the part to deform before relaxing the residual stresses. Furthermore, without the structural support of the base plate during the thermal cycle, the part becomes more prone to warping or distortion due to thermal expansion and contraction. On the other hand, heat treating a detached part allows for uniform thermal processing, resulting in more consistent deformation. Additionally, it could also reduce the influence of thermal expansion and contraction from the base plate on the part. Ultimately, the best approach can depend on the specific geometries and processes being used, so it's often necessary to conduct trials and validate the outcomes in the specific context.

To investigate different scenarios for both the dog bone and cruciform samples, we applied the simulation to evaluate two different process sequences. The resulting deformation data, illustrated in Fig 5.1, indicate that the timing of base plate removal in relation to HT has a significant effect on part deformation. This impact is evident even when maximum deformation happens at similar locations for both sequences. Specifically, removing the base plate before HT consistently results in lower deformation compared to removing it afterward.

For the dog bone sample, the final deformation is 0.64 mm when the base plate is removed after HT, whereas it is 0.58 mm when removed before. Similarly, for the cruciform sample, the final deformation is 1.01 mm after HT and 0.76 mm before. This reduction in deformation when the base plate is removed before HT suggests that this approach provides a more controlled thermal environment, effectively reducing residual stresses and overall deformation.

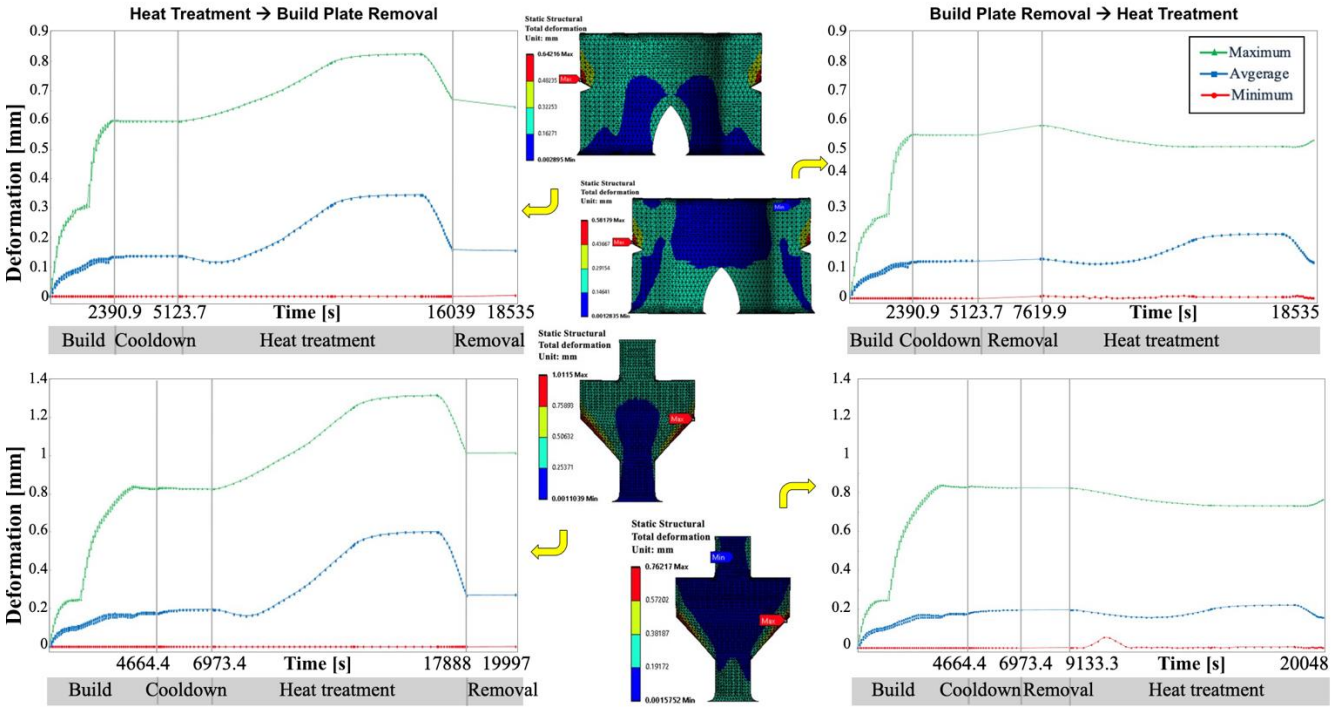

Figure 5-1. Comparing part deformation with two process sequences: removal from the base plate before versus after heat treatment, showing maximum (△), average (■), and minimum (○) values

Further analysis of the deformation graphs indicates that, in cases where the base plate is removed after HT, there is a significant increase in deformation during the HT step. This suggests that retaining the base plate during HT accentuates stresses and thermal gradients due to its bulk volume, resulting in more pronounced warping or distortion. In contrast, when the base plate is removed before HT, the deformation graph remains relatively stable throughout the process. This stability shows that removing the base plate beforehand allows for more uniform thermal processing, resulting in better managing thermal stresses and reducing deformation.

All in all, the results indicate that removing the base plate before HT leads to consistently lower deformation for both samples. For the dog bone, which has V-grooves that create stress concentrations, and the cruciform, with its discrete cross-sections, this method helps to control deformation by ensuring a more stable thermal environment. The reduced and more stable deformation further highlights the benefits of this approach in achieving improved dimensional accuracy and stability in AM processes.

Chapter 6

Conclusion

This thesis introduces a comprehensive integrated simulation process designed to predict crack locations in Laser Powder Bed Fusion (LPBF) samples both before and after stress relief heat treatment (HT).
The methodology includes coupled thermomechanical simulations to analyze stress distribution in dog bone and cruciform geometries, enabling the calculation of stress intensity factors at these sites. Subsequently, crack locations were determined based on stress intensity factors and the material's fracture toughness, and the crack location predictions were validated against printed samples.

The results show that specific geometric features, such as the discrete cross-sections in the cruciform and V-grooves in the dog bone samples, affects stress peak patterns and crack behavior during various stages of the process, including LPBF and stress relief HT. In the cruciform sample, the transition points between the discrete cross-sections experienced high stress concentrations, highlighting the importance of maintaining uniform cross-sections this geometry. Additionally, in the dog bone sample, the v-grooves exhibited high stress concentrations at different stages of the process, showing the impact of geometric features on the stress distribution throughout the process stages and the importance of proper sequencing.
The findings also indicates that process sequences affect the accuracy of the final geometry. Specifically, removing the base plate before heat treatment in both the cruciform and dog bone samples resulted in reduced deformation, which improved accuracy by enabling a more uniform thermal process and leading to more consistent deformation.

All in all, the study emphasizes how geometric design greatly influences stress distribution, impacting crack formation. The simulations developed in this research provide valuable tools for evaluating component designs prior to manufacturing. By predicting potential crack locations and

optimizing process sequences, engineers can assess designs ahead of fabrication to uncover potential crack sites and enhance the design, thus improving the structural integrity of LPBF components. The findings have broad applicability across various industries, offering a framework for improving additive manufacturing processes.

Future research can focus on incorporating real-world defects into simulation models. Advanced techniques for defect modeling and characterization could increase the accuracy of crack predictions and better represent the actual material behavior. Expanding the study to include a wider range of geometrical shapes and designs would offer valuable insights into how different features influence stress distribution and crack formation. This broader approach could improve the applicability of the findings across various additive manufacturing scenarios. Exploring alternative post-processing techniques, such as hot isostatic pressing (HIP), could also provide additional perspectives on their effectiveness in reducing crack formation and enhancing part quality. Finally, future research could also benefit from applying Elastic-Plastic Fracture Mechanics (EPFM) for crack simulation. This approach may offer a more detailed understanding of crack propagation under varying stress conditions.

Bibliography

[1] L. Zhang and H. Attar, "Selective Laser Melting of Titanium Alloys and Titanium Matrix Composites for Biomedical Applications: A Review ," *Adv Eng Mater*, vol. 18, no. 4, pp. 463–475, Apr. 2016, doi: 10.1002/adem.201500419.

[2] Y. Song, Y. Yan, R. Zhang, D. Xu, and F. Wang, "Manufacture of the die of an automobile deck part based on rapid prototyping and rapid tooling technology," *J Mater Process Technol*, vol. 120, no. 1–3, pp. 237–242, Jan. 2002, doi: 10.1016/S0924-0136(01)01165-7.

[3] M. Laleh, E. Sadeghi, R.I. Revilla, Q. Chao [a], N. Haghdadi, A.E. Hughes , W. Xu, I. Graeve, M. Qian , I. Gibson, M. Y. Tan "Heat treatment for metal additive manufacturing," *Prog Mater Sci*, vol. 133, p. 101051, 2023, doi: 10.1016/j.pmatsci.2022.101051.

[4] Z.J. Li, Z.H. Xiao, H.L. Zhang, H.L. Dai, W.F. Luo, and Z.W. Huang, "3D numerical modeling for thermo-mechanical behavior of additively manufactured titanium alloy parts with process-induced defects," *Int J Heat Mass Transf*, vol. 209, p. 124112, 2023, doi: 10.1016/j.ijheatmasstransfer.2023.124112.

[5] X. Yang, Y. Li, W. Jiang, M. Duan, D. Chen, and B. Li, "Ductile fracture prediction of additive manufactured Ti6Al4V alloy based on an extended GTN damage model," *Eng Fract Mech*, vol. 256, p. 107989, 2021, doi: 10.1016/j.engfracmech.2021.107989.

[6] X. Zhang, H. Chen, L. Xu, J. Xu, X. Ren, and X. Chen, "Cracking mechanism and susceptibility of laser melting deposited Inconel 738 superalloy," *Mater Des*, vol. 183, p. 108105, Dec. 2019, doi: 10.1016/j.matdes.2019.108105.

[7] N. Perevoshchikova, J. Rigaud, Y. Sha, M. Heilmaier, B. Finnin, E. Labelle, X. Wu, "Optimisation of selective laser melting parameters for the Ni-based superalloy IN-738 LC using Doehlert's design," Rapid Prototyp J, vol. 23, no. 5, pp. 881–892, Jan. 2017, doi: 10.1108/RPJ-04-2016-0063.

[8] W. Zhou, Y. Tian, D. Wei, Q. Tan, D. Kong, H. Luo, W. Huang, G. Zhu, D. Shu, J. Mi, B. Sun, "Effects of heat treatments on the microstructure and tensile properties of IN738 superalloy with high carbon content fabricated via laser powder bed fusion," J Alloys Compd, vol. 953, p. 170110, Aug. 2023, doi: 10.1016/j.jallcom.2023.170110.

[9] K. A. Shiyas and R. Ramanujam, "A review on post processing techniques of additively manufactured metal parts for improving the material properties," *Mater Today Proc*, vol. 46, pp. 1429–1436, 2021, doi: 10.1016/j.matpr.2021.03.016.

[10] D. Greitemeier, F. Palm, F. Syassen, and T. Melz, "Fatigue performance of additive manufactured TiAl6V4 using electron and laser beam melting," *Int J Fatigue*, vol. 94, pp. 211–217, Jan. 2017, doi: 10.1016/j.ijfatigue.2016.05.001.

[11] Nagesha. B. K, Vinodh. K, Amit. K. Tigga, S. Barad, and Anand. Kumar. S, "Influence of post-processing techniques on residual stresses of SLM processed HPNGV," *J Manuf Process*, vol. 66, pp. 189–197, Jun. 2021, doi: 10.1016/j.jmapro.2021.04.020.

[12] B. Vrancken, L. Thijs, J.-P. Kruth, and J. Van Humbeeck, "Heat treatment of Ti6Al4V produced by Selective Laser Melting: Microstructure and mechanical properties," *J Alloys Compd*, vol. 541, pp. 177–185, Nov. 2012, doi: 10.1016/j.jallcom.2012.07.022.

[13] G. Lesiuk, M. Szata, W. Blazejewski, A. M.P. de Jesus, J.F.O. Correia, *Struct. Integr. Fatigue Fail. Anal*: *Experimental, theoretical and numerical approaches*, vol. 25. Cham: Springer International Publishing, 2022. doi: 10.1007/978-3-030-91847-7.

[14] M. Gouge, P. Michaleris, E. Denlinger, and J. Irwin, “The Finite Element Method for the Thermo-Mechanical Modeling of Additive Manufacturing Processes,” in *Thermo-Mechanical Modeling of Additive Manufacturing*, Elsevier, 2018, pp. 19–38. doi: 10.1016/B978-0-12-811820-7.00003-3.

[15] T. B. Şirin and Y. Kaynak, “Prediction of residual stress and distortion in laser powder bed fusion additive manufacturing process of Inconel 718 alloy,” *Procedia CIRP*, vol. 99, pp. 330–335, 2021, doi: 10.1016/j.procir.2021.03.102.

[16] A. Shrivastava, S. Anand Kumar, and S. Rao, “A numerical modelling approach for prediction of distortion in LPBF processed Inconel 718,” *Mater Today Proc*, vol. 44, pp. 4233–4238, 2021, doi: 10.1016/j.matpr.2020.10.538.

[17] M. P. Sealy, G. Madireddy, C. Li, and Y. B. Guo, “Finite element modeling of hybrid additive manufacturing by laser shock peening,” in *2016 International Solid Freeform Fabrication Symposium*, University of Texas at Austin, 2016.[Online]: https://repositories.lib.utexas.edu/items/06c815c8-5c5c-4e4b-91b3-b7d0228fdf68

[18] Y. Wang, A. Sha, X. Li, S. Jiang, and W. Hao, “Numerical simulation of residual stresses in hot isostatic pressed SiC/GH4738 composites,” *Composites Part C: Open Access*, vol. 3, p. 100046, Nov. 2020, doi: 10.1016/j.jcomc.2020.100046.

[19] S. M. Afazov, S. Nikov, A. A. Becker, and T. H. Hyde, “Manufacturing chain simulation of an aero-engine disc and sensitivity analyses of micro-scale residual stresses,” *J. Adv. Manuf. Technol.*, vol. 52, pp. 279–290, 2011. doi: 10.1007/s00170-010-2707-2

[20] J. M. O’Brien, S. Montgomery, A. Yaghi, and S. M. Afazov, “Process chain simulation of laser powder bed fusion including heat treatment and surface hardening,” *CIRP J Manuf Sci Technol*, vol. 32, pp. 266–276, Jan. 2021, doi: 10.1016/j.cirpj.2021.01.006.

[21] Q.Y. Jin, D. Kang, K. Ha, J. H. Yu, and W. Lee, “Simulation of annealing process on AISI 316 L stainless steel fabricated via laser powder bed fusion using finite element method with creep,” *Addit Manuf*, vol. 60, p. 103255, Dec. 2022, doi: 10.1016/j.addma.2022.103255.

[22] X. Lu, C. Chen, G. Zhang, M. Chiumenti, M. Cervera, H. YYin, L. Ma, X. Lin “Thermo-mechanical simulation of annealing heat treatment of Ni-based GH4099 superalloy made by laser powder bed fusion,” *Addit Manuf*, vol. 73, p. 103703, Jul. 2023, doi: 10.1016/j.addma.2023.103703.

[23] X. Zhang, F. Martina, J. Ding, X. Wang, and S. Williams, “Fracture toughness and fatigue crack growth rate properties in wire arc additive manufactured Ti-6Al-4V,” *Fatigue Fract Eng Mater Struct*, vol. 40, no. 5, pp. 790–803, May 2017, doi: 10.1111/ffe.12547.

[24] Z. Jiang, J. Sun, F. Berto, X. Wang, and G. Qian, “Fatigue and Fracture Behavior of AlSi10Mg Manufactured by Selective Laser Melting: A Review,” *Physical Mesomechanics*, vol. 26, no. 4, pp. 367–390, Aug. 2023, doi: 10.1134/S102995992304001X.

[25] H. Liu, H. Yu, C. Guo, X. Chen, S. Zhong, L. Zhou, A. Osman, J. Lu “Review on Fatigue of Additive Manufactured Metallic Alloys: Microstructure, Performance, Enhancement and Assessment Methods,” *Advanced Materials*, Aug. 2023, doi: 10.1002/adma.202306570.

[26] C. Pei, D. Shi, H. Yuan, and H. Li, “Assessment of mechanical properties and fatigue performance of a selective laser melted nickel-base superalloy Inconel 718,” *Mater. Sci: A*, vol. 759, pp. 278–287, Jun. 2019, doi: 10.1016/j.msea.2019.05.007.

[27] K. Gruber, P. S. Ziółkowska, S. Dziuba, S. Duda, P. Zielonka, S. Seitl, G. Lesiuk “Fatigue crack growth characterization of Inconel 718 after additive manufacturing by laser powder

bed fusion and heat treatment," *Int J Fatigue*, vol. 166, p. 107287, Jan. 2023, doi: 10.1016/j.ijfatigue.2022.107287.
[28] W. Tang, Z. Tang, W. Lu, S. Wang, and M. Yi, "Modeling and Prediction of Fatigue Properties of Additively Manufactured Metals," *Acta Mechanica Solida Sinica*, vol. 36, no. 2, pp. 181–213, Apr. 2023, doi: 10.1007/s10338-023-00380-5.
[29] R. Verma, P. Kumar, R. Jayaganthan, and H. Pathak, "Extended finite element simulation on Tensile, fracture toughness and fatigue crack growth behaviour of additively manufactured Ti6Al4V alloy," *Theor. Appl. Fract. Mech*, vol. 117, p. 103163, Feb. 2022, doi: 10.1016/j.tafmec.2021.103163.
[30] M. Fielden and C. M. Davies, "Prediction of Residual Stresses and Stress Intensity Factors in Fracture Mechanics Samples Manufactured by Laser Powder Bed Fusion," in Vol *4: ASME*, Jul. 2021. doi: 10.1115/PVP2021-62996.
[31] H. T. Tran, X. Liang, and A. C. To, "Efficient prediction of cracking at solid-lattice support interface during laser powder bed fusion via global-local J-integral analysis based on modified inherent strain method and lattice support homogenization," *Addit Manuf*, vol. 36, p. 101590, Dec. 2020, doi: 10.1016/j.addma.2020.101590.
[32] H. T. Tran, Q. Chen, J. Mohan, and A. C. To, "A new method for predicting cracking at the interface between solid and lattice support during laser powder bed fusion additive manufacturing," *Addit Manuf*, vol. 32, p. 101050, Mar. 2020, doi: 10.1016/j.addma.2020.101050.
[33] L. Zhang, Y. Li, Q. Zhang, and S. Zhang, "Microstructure evolution, phase transformation and mechanical properties of IN738 superalloy fabricated by selective laser melting under different heat treatments," *Mater. Sci: A*, vol. 844, p. 142947, 2022, doi: https://doi.org/10.1016/j.msea.2022.142947.
[34] L. Rickenbacher, T. Etter, S. Hövel, and K. Wegener, "High temperature material properties of IN738LC processed by selective laser melting (SLM) technology," *Rapid Prototype J*, vol. 19, no. 4, pp. 282–290, Jan. 2013, doi: 10.1108/13552541311323281.
[35] "ANSYS Workbench Additive Manufacturing Analysis Guide Third-Party Software," 2020. [Online]. Available: http://www.ansys.com
[36] S. Weber, J. Montero, M. Bleckmann, and K. Paetzold, "A Comparison of Layered Tetrahedral and Cartesian meshing in Additive Manufacturing Simulation," *Procedia CIRP*, vol. 91, pp. 522–527, 2020, doi: 10.1016/j.procir.2020.02.209.
[37] G. G. Garrett and J. F. Knott, "The influence of compositional and microstructural variations on the mechanism of static fracture in aluminum alloys," *Metallurgical Transactions A*, vol. 9, no. 9, pp. 1187–1201, 1978, doi: 10.1007/BF02652242.
[38] X. Yu *et al.*, "Influence of post-heat-treatment on the microstructure and fracture toughness properties of Inconel 718 fabricated with laser directed energy deposition additive manufacturing," *Mater. Sci:A*, vol. 798, p. 140092, 2020, doi: 10.1016/j.msea.2020.140092.
[39] Chuan Guo, "An investigation of defects in the nickel-based superalloy IN738LC fabricated by laser powder bed fusion," Ph.D thesis, University of Birmingham, 2021. [Online]. Available: https://etheses.bham.ac.uk/id/eprint/11997/
[40] W. Zhou, Y. Tian, D. Wei, O. Tan, D. Kong, H. Luo, W. Huang, G. Zhu, D. Shu, J. Mi, B. Sun "Effects of heat treatments on the microstructure and tensile properties of IN738 superalloy with high carbon content fabricated via laser powder bed fusion," *J Alloys Compd*, vol. 953, p. 170110, Aug. 2023, doi: 10.1016/j.jallcom.2023.170110.

Appendix

Appendix A. Structural boundary condition

In order to simulate the removal of the sample from the base plate, three nodes need to be constrained. The constraints for the three nodes are as follows: Node 1 is constrained in all three directions (x, y, and z). Node 2 is constrained in the y and z directions, while Node 3 is constrained in the z direction. Fig. 1 indicates the constrained points for both geometries. The command for constraining three points is shown in Fig. 2 Appendix.

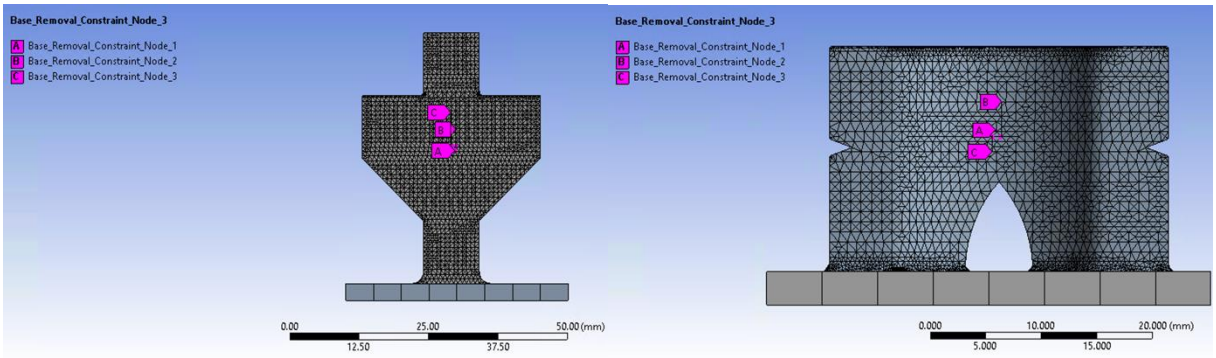

Figure. 1 Constrained point for both Cruciform and Dog bone geometry

```
d,Base_Removal_Constraint_Node_1,ux,%_fix%
d,Base_Removal_Constraint_Node_1,uy,%_fix%
d,Base_Removal_Constraint_Node_1,uz,%_fix%
d,Base_Removal_Constraint_Node_2,uy,%_fix%
d,Base_Removal_Constraint_Node_2,uz,%_fix%
d,Base_Removal_Constraint_Node_3,uz,%_fix%
```

Figure. 2 Commands for fixing three points in the base plate removal step

Appendix B. Importing stress and deformation data to fracture analysis accurately

To perform fracture analysis, it is important to transfer these stresses and deformation data accurately into a new static structural analysis within Ansys Workbench. The accuracy of this study heavily depends on data transfer, as the initiation and propagation of cracks rely on stress values. To transfer data, the solution from the previous analysis is typically linked to the setup of the subsequent analysis. However, in the case of an additive manufacturing module, this linking is not possible in ANSYS. The most accurate approach for transferring data from the additive manufacturing analysis to another analysis involves a three-step process. Initially, exporting the CDB mesh file to ensure that the node-base data can be precisely mapped to the same mesh and node ID. Note the advantage of using CDB file is that CDB file format is meshed geometry file; therefore, the stress information based on node ID can be mapped on this file without any error. Subsequently, exporting the data based on the node ID. Finally, importing the mesh file into an external model and establish a connection with the subsequent analysis. These three-step procedures are explained further as follows.

1- Exporting CDB mesh file

To export the CDB mesh file, all the bodies (build part and base plate) in the analysis should be separately selected in name selection bodies. Also, a name selection should be selected containing all of the bodies. The command to export CDB file should be added to the solution. After solving the analysis, the CDB files will be in the working directory. The command to export CDB file is shown in Fig. 3.

```
/PREP7

CMSEL,s,Body1
CDWRITE,db,mesh_Body1,cdb

CMSEL,s,Body2
CDWRITE,db,mesh_Body2,cdb

CMSEL,s,Bodyall
CDWRITE,db,mesh_Bodyall,cdb
```

```
ALLSEL

/solution
/EOF
```

Figure. 3 Commands to export CDB mesh file

2- Exporting Stress and deformation data

When exporting stress data, it is essential to export normal and shear stress values separately as an Excel file. It is important to note that the data should be exported based on the node ID not the x, y, z node location. Likewise, deformation data should be exported individually, including deformations along the x, y, and z axes.

3- Importing data to static structural analysis

To import data for fracture analysis, it is necessary to link an external model and two external data to the static structural analysis, as shown in Fig. 4. Once the analysis is opened, the appropriate material should be chosen and subsequently the external data should be loaded onto the corner nodes of the geometry.

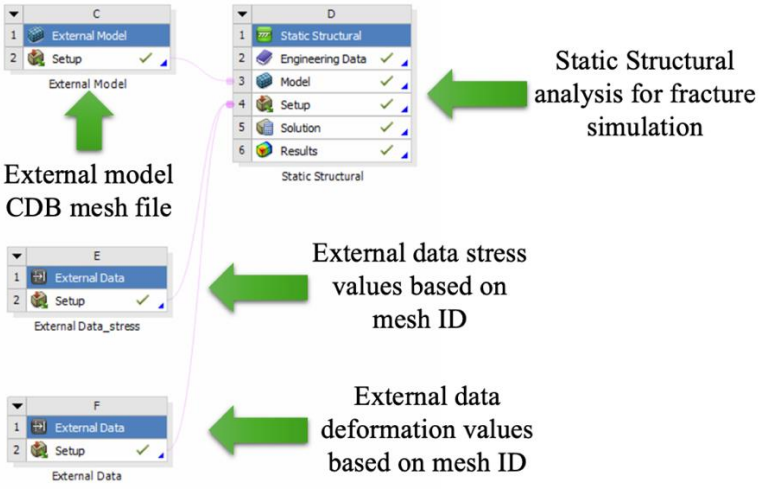

Figure. 4 Overall workflow for importing CDB mesh file and external data

After the data has been loaded onto the geometry, it is important to conduct a comparison between the specified nodes and the mapped nodes to confirm the accurate alignment of all data with the geometry.